



Revolutionising Detection Systems For Intercepting The Illicit Transportation Of Radioactive Materials Concealed Within Shipping Containers

Euan L. Connolly 
Interface Analysis Centre
University of Bristol, UK
e.connolly@bristol.ac.uk

Samuel R. White
Interface Analysis Centre
University of Bristol, UK

Dean T. Connor
Interface Analysis Centre
University of Bristol, UK

Peter G. Martin 
Interface Analysis Centre
University of Bristol, UK

ABSTRACT

As the international community moves towards a greater nuclear power provision as part of a low-carbon energy mix, there are consequently expanding opportunities for the loss or theft of such materials that could be fabricated into improvised nuclear explosive or radiological dispersal devices. To prevent these dangerous materials falling into the hands of malicious actors, it is essential to deter and detect its illicit transportation when concealed within shipping containers. As these constitute a significant proportion of global trade, implementing a robust shipping container screening system at seaports represents a crucial national security consideration. For existing screening systems, shipping containers are driven through radiation portal monitors comprising plastic scintillators for gamma detection and separate, typically ^3He -based, neutron detectors. These polyvinyl toluene plastic-based scintillators enable current screening systems to meet detection sensitivity standards owing to their economical manufacturing in large sizes - producing high geometric efficiency detectors, however, their poor spectral resolution fundamentally limits the screening process to making binary 'source' or 'no source' decisions, necessitating a secondary, and more thorough, inspection phase for suspect containers. The next generation of shipping container screening systems should be comparable in throughput and cost to existing systems, but have the energy resolution to identify specific radionuclides and the spatial resolution to localise their position within a container, therefore expediting the screening process and eliminating the requirement for the time-consuming and costly secondary inspection phase. By simulation using Monte Carlo/deterministic methods and experimental validation, this work evaluates the material and configurational properties of detection systems, alongside the data collection and processing algorithms employed, to develop prospective shipping container screening systems capable of characterising concealed gamma-emitting sources. One research area of particular interest is the incorporation of inorganic scintillator detectors into lifting equipment employed at ports to load and unload containers from ships. Such detection infrastructure provides an opportunity to take extended measurements of a shipping container at short stand-off distances using geometrically favorable detector configurations that, combined with advanced data processing algorithms, enable the enhanced isotopic and locational characterisation of concealed sources.

I. INTRODUCTION

The detonation of improvised nuclear explosive devices (INEDs) or radiological dispersal devices (RDDs) by malicious actors has the potential to cause severe loss of human life alongside disastrous economic and psychological damage to society [1, 2]. While events relating to the trafficking or malicious use of radioactive materials required to fabricate INEDs and RDDs remain relatively low, with 29 incidents reported to the International Atomic Energy Agency (IAEA) Incident and Trafficking Database (ITDB) between 2015 and 2019 [3], it is clear that quantities of these materials exist outside of regulatory control. Additionally, the ITDB fails to account for undetected or unreported incidents, such as black market trading, and with a global trend towards nuclear power generation, the opportunity for the loss and theft of nuclear and radioactive materials is only increasing.

To construct an INED, complex requisite knowledge and access to special nuclear materials, such as ^{239}Pu and highly enriched uranium (HEU) are required, whereas RDDs can be easily fabricated using any available radioactive materials, with isotopes such as ^{137}Cs , ^{60}Co and ^{90}Sr identified as posing the greatest security risk based on factors such as availability, half-life and common physical form [2]. For identifying and deterring the illicit transportation of such nuclear or radioactive materials in significant quantities, robust detection infrastructure and protocols are essential. The obvious location for detection infrastructure is at seaports, with more than 80% of the world's goods transported by sea, and 811 million twenty-foot equivalent units of shipping containers being transported through ports globally in 2019 [4]. Screening shipping containers for concealed radioactive or nuclear materials presents obvious difficulties; the high throughput nature of seaport logistics limits the time available to inspect individual containers and the cargo materials and their packing provides intrinsic shielding to concealed sources.

The most widely used technique for screening containerised freight involves driving shipping containers, mounted on flatbed trucks, through radiation portal monitors (RPMs) comprised of two panels of radiation detectors straddling a traffic lane [5]. Typically, plastic scintillator radiation detectors are used in RPMs to detect the gamma radiation emitted by concealed radioactive sources as they can be affordably manufactured into large area ($\sim 1\text{ m}^2$) panels contributing to the efficiency of the detection systems by maximising the solid angle from the source subtended by the scintillator detectors, or the geometric efficiency. Implementing high-efficiency radiation detectors is essential for detecting concealed sources due to the short transit time of a container through an RPM; to detect concealed sources with a high likelihood, the number of radiation detection events registered by an RPM that originate from the source must be maximised. Due to the high density of ^1H with which high energy transfer p-n elastic scattering events can occur, plastic-based materials are intrinsically efficient for fast neutron detection, however, separate neutron detectors, such as ^3He gas filled proportional counters, are normally used in RPMs to achieve high-efficiency across a range of incident neutron energies.

Limitations with current shipping container screening infrastructure arise from the extremely low energy resolution of plastic scintillators detectors, meaning RPMs act only as a 'tripwire' to necessitate a secondary screening process. As well as causing RPMs to be susceptible to false alarms due to naturally occurring radioactive materials (NORM) and medical isotopes, the subsequent screening phase costs operational and human resources and causes delays. To mitigate against the low energy resolution of plastic scintillators, various methods have been developed to discriminate between different types of cargo, e.g. NORM, medical sources and threat sources, based on the distribution of counts in the spectra measured by a PVT detector [6]. However, there

remains considerable scope for the development of shipping container screening systems capable of radionuclide identification and location within a single, automated inspection.

One alternative method for shipping container screening is the incorporation of radiation detectors into port lifting equipment, such that containers can be screened during their movement through a port or during the (un)loading of seafaring transport vessels with spreader-bar cranes. In addition to having minimal or no impact on port operations, such a screening system would minimise the stand-off distance between the container and detectors, increase the amount of time available to screen the container, and offer a reduction in the naturally occurring radioactive background count rate [7, 8]. A longer measurement time and reduced stand-off distance would allow for reduced area, higher energy resolution radiation detectors, such as NaI(Tl) inorganic scintillator crystals, to be used; improving the radionuclide identification capability of the system and hence its capability to discriminate between legitimate and nuisance alarms. Multiple measurements obtained by a distributed array of radiation detectors on the top surface of a container would additionally possess information about the location of a concealed source within a container.

Despite the aforementioned benefits of incorporating radiation detectors into port lifting equipment, the intrinsic one-sided nature of such a screening process fundamentally limits its sensitivity compared to two-sided drive-through screening processes, such as RPMs. The constraint of only performing measurements from one side of a shipping container is a contributing factor to the lack of widespread implementation of spreader-bar radiation detection systems (SBRDs) in the face of past commercial availability [9]. A 2010 study into SBRDs carried out by Ely *et al.* [8] for the U.S. Department of Energy identifies the limitations of a one-sided SBRD, although the authors suggest that advanced algorithmic approaches used to process the measurements may be capable of increasing the sensitivity of SBRDs.

The aim of this work is to experimentally demonstrate the capability of an algebraic reconstruction technique (ART) iterative algorithm to localise radioactive point sources in three dimensions based on models of detector response and radiation measurements in a limited number of two dimensional planes. By demonstrating that such an ART algorithm is capable of source localisation using one-sided measurements, there is scope to investigate its use and potential to improve the sensitivity of SBRDs. This work should, therefore, be considered as a ‘proof of principle’ for the use of ART algorithms in the processing of SBRD measurements.

II. ALGEBRAIC RECONSTRUCTION ALGORITHMS

Iterative techniques provide a method for source localisation and are widely used in remote sensing applications, such as single-photon emission computed tomography (SPECT) and radio astronomy [10]. ART algorithms were initially used for image reconstruction in medical imaging, but more recently ART techniques have been applied to radioactive source localisation problems; White *et al.* [11] successfully employed a randomised ART method to localise radioactive sources in two-dimensions using an experimentally determined detector response function (DRF) in three-dimensions. Other forms of ART, particularly multiplicative ART iterative methods, are used to find the maximum likelihood solution in moving and static radioactive source localisation problems [12, 13, 14].

The purpose of using ART is to solve the set of linear equations given by;

$$\mathbf{b} = \mathbf{Ax} \quad (1)$$

where in the context of this work, \mathbf{b} is the set of I measurements made by a radiation detector, \mathbf{x} is the unknown radioactive source distribution discretised into J voxels in three dimensional space,

and \mathbf{A} is the $I \times J$ projection matrix, or DRF, that maps the physical source distribution space onto the measurement space [10]. Due to noise and measurement errors in \mathbf{b} , the system of equations defined by (1) is likely inconsistent and so has no exact solutions [15]. In iteratively solving (1), the aim is to find an approximate solution, such as the least squares solution that minimises the Euclidean norm $\|\mathbf{Ax} - \mathbf{b}\|_2$ [10].

In this work, a randomised ART is utilised with the constraint that $I > J$, such that (1) is over-determined in an attempt to achieve fast convergence to the true solution [16]. The solution is updated in each iteration based on the difference between the current solution evaluated at a single, randomly selected, measurement position, and the measurement at that position, b_i . Mathematically this is expressed as;

$$\mathbf{x}^{k+1} = \mathbf{x}^k + \lambda (b_i - (\mathbf{a}_i \cdot \mathbf{x}^k)) \frac{\mathbf{a}_i}{\|\mathbf{a}_i\|_2^2} \quad (2)$$

where k is the iteration number, λ is a relaxation parameter, \mathbf{a}_i denotes the i 'th row of the matrix \mathbf{A} , the \cdot operator represents the inner product and $\|\cdot\|_2$ represents the Euclidean norm [17]. By tuning the relaxation parameter the performance of the reconstruction and the rate of convergence of the algorithm are affected; strong under-relaxation ($\lambda < 1$) is proposed to achieve convergence to a least squares solution in the inconsistent case [10, 18]. In other work, White et al. [11] used a relaxation parameter that decreases as k increases, such that the convergence rate is initially prioritised.

Considering prior knowledge of the unknown radioactive source distribution, \mathbf{x} , additional constraints can be set. The first is a positivity constraint which prevents negative (non-physical) source activity in a single voxel; $x_j = \max\{x_j, 0\}$ for each x_j in \mathbf{x} . Secondly, assuming the concealed source distribution consists of a small and finite number of approximate point sources and zero background the resultant vector, \mathbf{x} , should be sparse (have a large number of zero entries) [12].

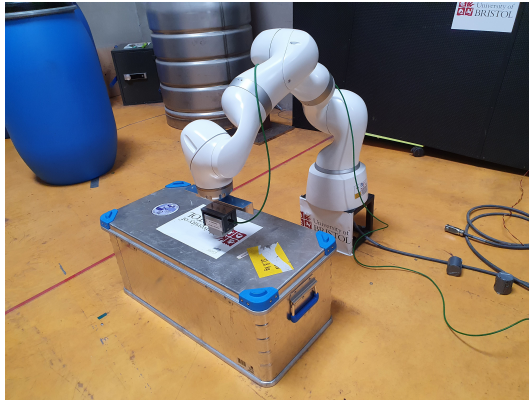
III. EXPERIMENTAL DATA AND ALGORITHM IMPLEMENTATION

A. Measurements

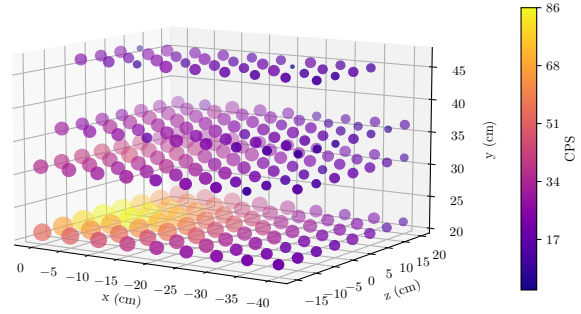
The data in this work was acquired using a robotic arm based radiation survey methodology, similar to work previously demonstrated in [19]. Five datasets were measured each consisting of raster scans in fixed planes above a 36 kBq ($\pm 10\%$) ^{137}Cs contaminated sediment source contained in a cylindrical perspex container of height and diameter 5×5 cm. A full description of the datasets is shown in Table I; an aluminium container was used in datasets 1-4 was to mimic an intermodal container although the attenuation factor it introduces is minimal (attenuation to 96% from 2 mm

Dataset	Description	Source coord. (cm)	Raster plane y coord. (cm)	Measurements
1	Source at center of aluminium case & edge of raster.	(0.0, -5.0, 0.0)	{21.0, 31.0, 36.0, 46.0}	242
2	Source at center of aluminium case & edge of raster.	(0.0, -5.0, 0.0)	{21.0, 22.0, 24.0}	214
3	Source off-center of aluminium case & slightly off-center of raster.	(-16.3, -5.0, 7.6)	{21.0, 22.0, 24.0, 25.0}	379
4	Source off-center of aluminium case & slightly off-center of raster.	(-16.3, -5.0, 7.6)	{20.0, 25.0, 30.0}	188
5	No aluminium case, source at edge of raster pattern	(0.0, 0.0, 0.0)	{4.0, 7.0, 9.0, 12.0, 14.0, 17.0, 19.0}	611

Table I: Description of raster scan datasets. Coordinates are relative to the center of the aluminium case.



(a)



(b)

Fig. 1: (a) Hamamatsu C12137-01 detector mounted on a robot arm manipulator performing a raster scan, and (b) 662 keV photopeak CPS for dataset 1, both colour and size of marker are scaled by the CPS.

of Al at 662 keV). The raster scan was conducted over one half of the aluminium container shown in Figure 1a, covering an approximately 40×40 cm area in the xz plane in steps of 5 cm. A Hamamatsu C12137-01 detector with a $3.8 \times 2.5 \times 3.8$ cm CsI(Tl) scintillating crystal was used in this work, selected for its sensitivity in the 662 keV range and reasonable energy resolution (8.5% at 662 keV) [20]. At each measurement position ten seconds of spectra were acquired and the data was processed to extract the count rate (CPS) in the 662 keV photopeak using a linear background model in the photopeak region and a constant detector dead-time correction; the resultant CPS for dataset 1 are shown in Figure 1b.

B. Detector Response Function Model

To approximately model the DRF, Monte Carlo based software under development at the University of Bristol was used. The method involves defining the spatial region occupied by the cuboid scintillating crystal in the detector, or the detector region, with six intersecting planes. At every point in a regular grid beneath the detector region the geometric efficiency of the detector was found by randomly sampling particle trajectories and determining the fraction which intersect the detector region.

In this work the DRF was evaluated at $27 \times 16 \times 17$ grid points spanning $160 \times 75 \times 90$ cm; the resultant DRF is shown for two distances below the detector center in Figure 2. Due to the large size of the parameter space and the inverse square law dependence of the DRF, contributions to the DRF at large distances away from the detector are minimal and thus the whole xz parameter space is not plotted in Figure 2. At each of the 7,344 grid points 10^5 particle trajectories were randomly sampled from a conic section directed towards and including the entire detector region. The computation of the DRF took approximately 60 minutes using 30 threads on a high performance computation architecture at the University of Bristol, though it is expected that optimisation of the code could significantly reduce this time.

As well as a correction factor to account for the angular restriction of the sampled particle trajectories, the DRF values were multiplied by a constant factor to include the attenuation effect

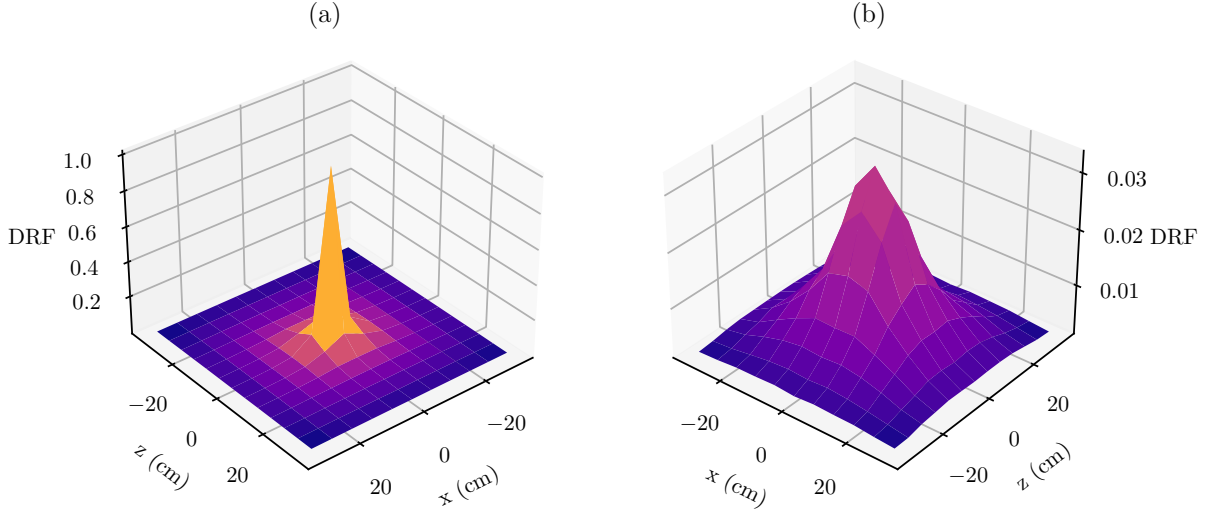


Fig. 2: Central region of the normalised DRF evaluated for a detector centred at $(0, 79, 0)$. DRF values are shown at (a) $y = 77.5$ cm, or 1.5 cm below the detector center and (b) $y = 67.5$ cm, or 11.5 cm below the detector center.

of the 2 mm thick aluminum container (for datasets 1-4) and a detector-to-grid-point-distance dependent factor accounting for the attenuation in air. The model did not account for attenuation caused by the detector crystal housing, nor the plastic detector mount seen in Figure 1a. Intrinsic efficiency of the detector was also assumed constant for all particle trajectories, although in practice this is affected by the path length of a particle track through the detector. While further improvements to the accuracy of the DRF could be made by accounting for the ignored attenuation factors and trajectory dependent intrinsic efficiency, the simplified DRF is expected to be sufficient for the demonstrative requirements of this work.

C. Algorithm Implementation And Performance Assessment

The algorithm in this work was implemented in Python 3.9 on a laptop computer with an i7 4 core processor and 16 GB of RAM. For all datasets the average run times for 10^6 iterations of the randomised ART algorithm were 183 s, however, significant reductions in computation time could be achieved through the optimisation of the Python code.

The relaxation parameter and number of iterations were 0.01 and 10^6 , respectively. Strong under-relaxation was used to ensure that the algorithm converged exponentially, therefore making it easier to confirm convergence. A consequence of using under-relaxation was that a large number of iterations, and hence greater computation time, was required to reach the approximate solution. The algorithm was initially run with the sparsity constraint $x_j = 0$ if $x_j < s \times \max(x)$ where $s = 0.01$ or 0.1, however, the algorithm consistently under-performed compared to the case with a positivity constraint, which was used henceforth. The solution was defined on $180, 6.2 \times 5.0 \times 5.6$ cm voxels directly below the measurement space and the initial solution, \mathbf{x}^0 , was a zero vector of length 180.

To assess the performance of the algorithm it must be shown to converge and be comparable to the true solution. In order to demonstrate convergence the norm $\|\mathbf{b} - \mathbf{Ax}\|_2$ was found after every 40,000th iteration; the average and standard deviation of the last five calculated norms were used as an

indicator of convergence. Additionally, by plotting $\|\mathbf{b}-\mathbf{Ax}\|_2$ against iteration number, a visual check was used to verify the exponential convergence expected with strong under-relaxation and rule out semi-convergence. Since the algorithm randomly samples measurements, six repeat implementations were performed for each dataset in order to ensure the algorithm converged irrespective of the measurement selection order.

To compare the approximate solution output by the algorithm to the true solution, the Euclidean norms $\|\mathbf{x}_{true}-\mathbf{x}\|_2$ (solution norm) and $\|\mathbf{r}_{true}-\mathbf{r}_{w,av}\|_2$ (localisation error) were used, where \mathbf{x}_{true} is the true solution, \mathbf{r}_{true} is the true position of the source and $\mathbf{r}_{w,av}$ is the average position of the solution voxels weighted by the counts in each voxel. The point source approximation of the true solution, described by the vector \mathbf{x}_{true} , is zero at every solution voxel except for the voxel containing the source, where the value is equal to the activity or CPS of the source. In the case where the DRF used in (2) is not normalised, the algorithm is expected to return the activity of the source (~ 36 kBq) but this will not be the case for a normalised DRF. While the solution norm evaluates the absolute accuracy of the algorithm, the localisation error provides an alternative metric that identifies equivalent/approximate solutions. Another metric, $\text{std}(\mathbf{r}_{w,av})$, the weighted standard deviation of $\mathbf{r}_{w,av}$ is a measure of the spatial distribution of the solution, effectively defining the precision of the solution.

IV. RESULTS AND DISCUSSION

Considering the data in Table II the algorithm was seen to converge for each dataset, with the standard deviation of $\|\mathbf{b}-\mathbf{Ax}\|_2$ evaluated at the last five 40,000th iterations being on the order of 1% averaged over the six repeats for each dataset. Figures 3d and 4b show typical convergence plots for the datasets; on inspection the convergence appears to be exponential as was expected with strong under-relaxation. Additionally, the low uncertainties associated with the repeat calculations of the localisation error and $\text{std}(\mathbf{r}_{w,av})$ indicated that the algorithm converged to the same average solution, regardless of the measurement selection order.

Dataset 5, which represented the ‘best’ dataset with the shortest source-to-detector distances and the largest number of measurements, returned the best results. Figure 3 shows the solution for dataset 5 after 10, 10⁴ and 10⁶ iterations; the count weighted spatial spread, $\text{std}(\mathbf{r}_{w,av})$, of the solution after 10⁶ iterations was 6.44 ± 0.28 cm, significantly lower than for datasets 1-4 (see Table II) indicating that the algorithm was able to more precisely localise the source with measurements of the form in dataset 5. The localisation error for dataset 5 was also low, being within 6 cm including the errors associated with the finite dimensions of the ¹³⁷Cs source and the use of a simplified DRF.

The solution norms, $\|\mathbf{x}_{true}-\mathbf{x}\|_2$, shown in Table II suggest that dataset 5 performed worse than datasets 1-4, however, this was a consequence of the inability of the algorithm to localise the source to the exact voxel, meaning the norm is dominated by the 36 kBq entry in \mathbf{x}_{true} . Even

Dataset	$\ \mathbf{b}-\mathbf{Ax}\ _2$ (CPS)	sum(\mathbf{b}) (CPS)	$\ \mathbf{x}_{true}-\mathbf{x}\ _2$ (Bq)	sum(\mathbf{x}) (Bq)	$\ \mathbf{r}_{true}-\mathbf{r}_{w,av}\ _2$ (cm)	$\text{std}(\mathbf{r}_{w,av})$ (cm)
1	79 ± 1	7,095	36,164	$38,462 \pm 270$	4.02 ± 0.08	21.34 ± 0.05
2	50 ± 1	9,307	35,838	$27,291 \pm 64$	10.66 ± 0.02	18.72 ± 0.03
3	84 ± 1	13,305	35,888	$32,618 \pm 29$	5.98 ± 0.03	20.46 ± 0.02
4	75 ± 1	8,982	35,758	$40,943 \pm 117$	3.31 ± 0.02	20.44 ± 0.01
5	1858 ± 31	175,382	45,118	$47,367 \pm 131$	5.64 ± 0.05	6.44 ± 0.28

Table II: Algorithm performance metrics for datasets 1-5 averaged over six repeats. Error on $\|\mathbf{b}-\mathbf{Ax}\|_2$ is the average standard deviation of the last five evaluations of $\|\mathbf{b}-\mathbf{Ax}\|_2$ in each repeat.

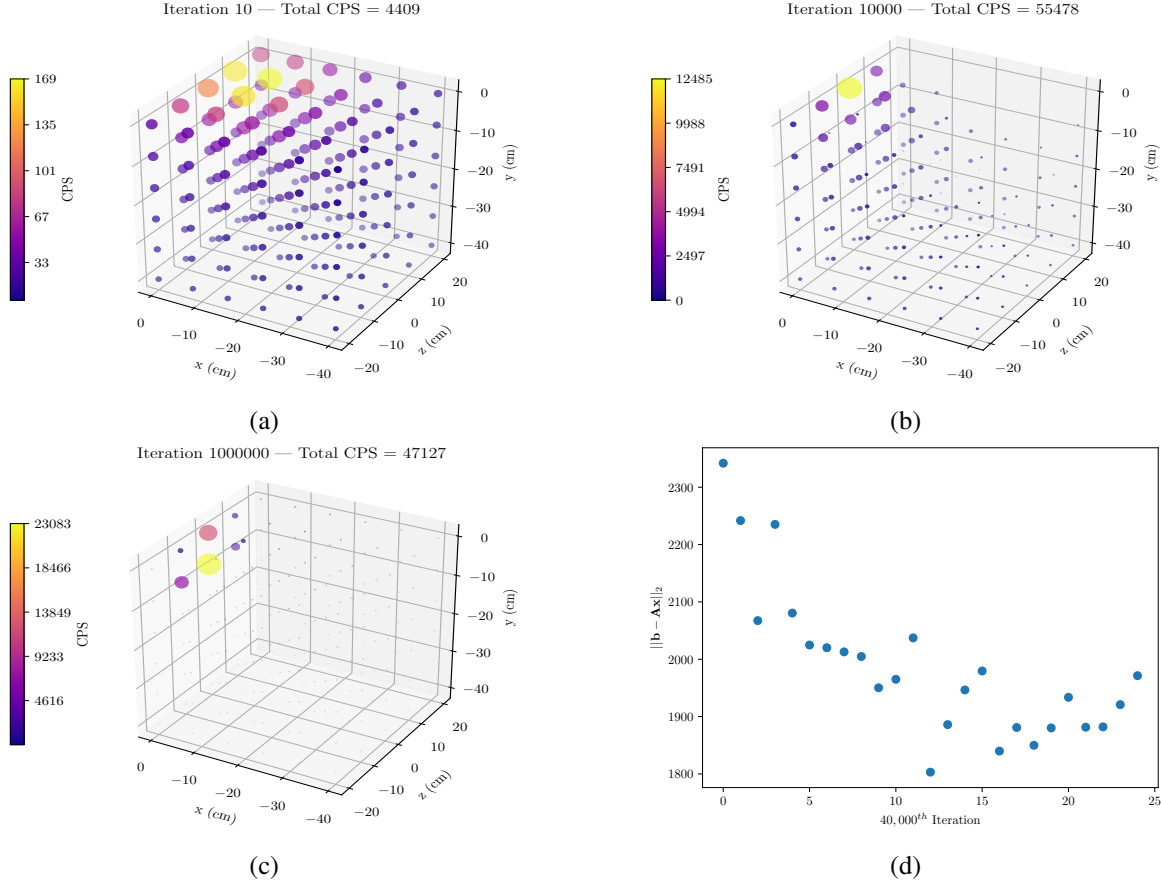


Fig. 3: Solution of the randomised ART algorithm for dataset 5 after (a) 10, (b) 10^4 and (c) 10^6 iterations and (d) the corresponding convergence plot. Marker size and colour in (a), (b) and (c) are scaled by the CPS.

though the solution activities were of the correct order of magnitude, ranging from 27 to 47 kBq across the datasets, this is not reflected in the solution norm as in datasets 1-4 the activity is more homogeneously distributed across the solution, meaning \mathbf{x}_{true} dominated the norm, and in dataset 5 there is a large activity contribution from an adjacent voxel, resulting in an increase in the solution norm. Consequently, the localisation error, count weighted spatial distribution of the solution, and sum of the solution were more useful metrics for assessing the algorithm performance.

Figure 4 shows the solution for dataset 1 after 10^6 iterations. While the solution was dispersed across the solution space, with $\text{std}(\mathbf{r}_{w,av}) = 21.34 \pm 0.05$ cm, the localisation error itself is low, being within the dimensions of a single solution voxel. A similar result was obtained with dataset 4, which also has variation in the raster plane y coordinate on the order of 10 cm. Considering the results for datasets 3 and 4, with the same source position, taking more measurements (379 and 188, respectively) did not better the performance of the algorithm, rather the localisation error was improved by taking measurements at more widely spaced y coordinates (heights). This is verified by dataset 2, with the lowest y variation and largest localisation error. The benefit of obtaining more measurements is that the solution space can be split into smaller voxels while (1) remains over-determined; improvements associated with varying the solution discretisation were not explored in

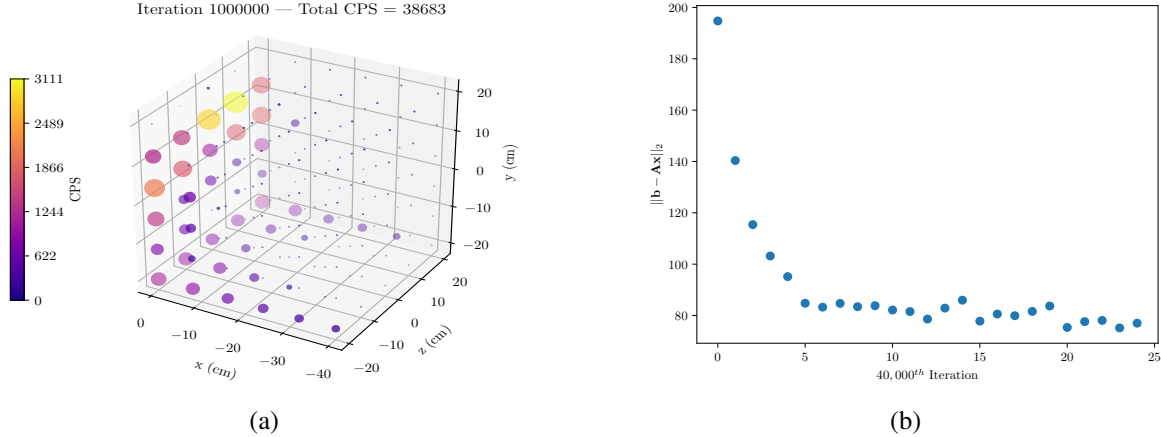


Fig. 4: (a) Solution of the randomised ART algorithm for dataset 1 after 10^6 iterations and (b) the corresponding convergence plot. Marker size and colour in (a) are scaled by the CPS.

this work, rather the solution voxels were kept the same for each dataset to facilitate comparison.

V. CONCLUSION

The randomised ART algorithm used in this work is capable of localising a radioactive source in three dimensions using measurements in a limited number of two dimensional planes, but the precision of the solution is strongly data dependent. The algorithm performs better when measurements are taken close to the source and when the y spread of the measurement planes is larger. While both these criteria are met by dataset 5, such measurements are not guaranteed using a SBRD system as sources may be located anywhere within the container. Datasets 1-4 represent more analogous measurements to those that would be taken with a SBRD system and while their solutions are less precise, being more evenly distributed across the solution space, the average solution captures the properties of the source. The localisation error was consistently below 11 cm, which can at least reduce the possible location of a source to a subsection of a container, and the algorithm predicted the activity of the source to the correct order of magnitude.

To improve the performance of the randomised ART algorithm and its suitability for SBRD systems, future efforts should investigate means of reducing the spread of the solution. Enforcing sparsity on the solution vector is one such means that warrants further investigation. The crude sparsity constraint implemented in this work did not improve the performance, however, alternative methods of enforcing sparsity may yield better results [12].

In this work single, point-like sources have been considered, whereas in reality multiple distributed and shielded sources may be present. Future work should also assess the performance of the algorithm with multiple point sources, although its effectiveness will likely depend the minimisation of the spread of the solution observed in this work, such that multiple sources can be resolved. For shielded sources the problem is complicated further but for a SBRD system would likely require multiple DRFs defined for different common scenarios, which are selected based on the weight of a container and its stated contents.

Overall, the results of the randomised ART algorithm are promising for one-sided shipping container screening using SBRD systems, although a full scale proof of principle is clearly required to assess the sensitivity at the distance scales typical of full sized intermodal containers. Additionally, the effect of the footprint of the SBRD must be considered as the detectors are constrained to be

attached to the spreader bar. Although extended measurement times will be possible when the container is being transported by the spreader bar crane, to achieve measurements at a range of y coordinates (heights) above the container data acquisition during the approach of the spreader bar to the top surface of the container will be crucial, whether sufficient data can be collected in the lowering time of the spreader bar onto the container requires further investigation.

ACKNOWLEDGMENTS

This work was carried out using the computational facilities of the Advanced Computing Research Centre, University of Bristol - <http://www.bristol.ac.uk/acrc/>.

REFERENCES

- [1] H. Rosoff and D. Von Winterfeldt, "A risk and economic analysis of dirty bomb attacks on the ports of Los Angeles and Long Beach," *Risk Analysis*, vol. 27, no. 3, pp. 533–546, 2007.
- [2] C. D. Ferguson, W. C. Potter, L. S. Spector, A. Sands, and W. C. Potter, *The Four Faces of Nuclear Terrorism*. Taylor & Francis Group, 2005.
- [3] IAEA, "IAEA Incident and Trafficking Database (ITDB) Fact Sheet 2020," *IAEA Incident and Trafficking Database (ITDB)*, p. 6, 2020.
- [4] United Nations Conference On Trade And Development, "Review Of Maritime Transport 2020," tech. rep., 2020.
- [5] R. T. Klann, J. Shergur, and G. Mattesich, "Current State of Commercial Radiation Detection Equipment for Homeland Security Applications," *Nuclear Technology*, vol. 168, pp. 79–88, 10 2009.
- [6] J. Ely, R. Kouzes, J. Schweppe, E. Siciliano, D. Strachan, and D. Weier, "The use of energy windowing to discriminate SNM from NORM in radiation portal monitors," *Nuclear Instruments and Methods in Physics Research, Section A: Accelerators, Spectrometers, Detectors and Associated Equipment*, vol. 560, pp. 373–387, 5 2006.
- [7] M. D. Grypp, C. M. Marianno, J. W. Poston, and G. C. Hearn, "Design of a spreader bar crane-mounted gamma-ray radiation detection system," *Nuclear Instruments and Methods in Physics Research Section A: Accelerators, Spectrometers, Detectors and Associated Equipment*, vol. 743, pp. 1–4, 2014.
- [8] J. H. Ely, E. D. Ashbaker, M. T. Batdorf, J. E. Baciak, W. K. Hensley, K. D. Jarman, S. M. Robinson, G. A. Sandness, and J. E. Schweppe, "Spreader-Bar Radiation Detection System Enhancements: A Modeling and Simulation Study," tech. rep., Pacific Northwest National Lab. (PNNL), Richland, WA (United States), 2012.
- [9] Veritainer Asset Holding, "Veritainer," 2014.
- [10] C. L. Byrne, *Applied Iterative Methods*. New York: A K Peters/CRC Press, 1st ed., 2007.
- [11] S. R. White, K. T. Wood, P. G. Martin, D. T. Connor, T. B. Scott, and D. A. Megson-Smith, "Radioactive Source Localisation via Projective Linear Reconstruction," 2021.
- [12] D. J. Lingenfelter, J. A. Fessler, and Z. He, "Sparsity regularization for image reconstruction with Poisson data," *Computational Imaging VII*, vol. 7246, p. 72460F, 2009.
- [13] B. Deb, "Iterative estimation of location and trajectory of radioactive sources with a networked system of detectors," *IEEE Transactions on Nuclear Science*, vol. 60, no. 2, pp. 1315–1326, 2013.
- [14] D. Hellfeld, T. H. Y. Joshi, M. S. Bandstra, R. J. Cooper, B. J. Quiter, and K. Vetter, "Gamma-Ray Point-Source Localization and Sparse Image Reconstruction Using Poisson Likelihood," *IEEE Transactions on Nuclear Science*, vol. 66, no. 9, pp. 2088–2099, 2019.
- [15] C. Popa and R. Zdunek, "Kaczmarz extended algorithm for tomographic image reconstruction from limited-data," *Mathematics and Computers in Simulation*, vol. 65, no. 6, pp. 579–598, 2004.
- [16] T. Strohmer and R. Vershynin, "A Randomized Kaczmarz Algorithm with Exponential Convergence," *Journal of Fourier Analysis and Applications*, vol. 15, no. 2, p. 262, 2008.
- [17] D. Needell and J. A. Tropp, "Paved with good intentions: Analysis of a randomized block Kaczmarz method," *Linear Algebra and Its Applications*, vol. 441, pp. 199–221, 2014.
- [18] Y. Censor, P. P. B. Eggermont, and D. Gordon, "Strong Underrelaxation in Kaczmarz 's Method for Inconsistent Systems," *Image Processing*, vol. 92, pp. 83–92, 1983.
- [19] S. R. White, D. A. Megson-Smith, K. Zhang, D. T. Connor, P. G. Martin, C. Hutson, G. Herrmann, J. Dilworth, and T. B. Scott, "Radiation Mapping and Laser Profiling Using a Robotic Manipulator," *Frontiers in robotics and AI*, vol. 7, p. 499056, 11 2020.
- [20] Hamamastu Photonics K. K., "CS12137-01 Radiation Detection Module."